Supplementary Materials for

Mechanical decoupling on multiscale heterointerface for customizable and robust strain sensors

Lang Wang[1,2#], Yuyu Gao[4,5#], Chenbo Wu[1,2], Xinge Yu[4,5,6,7]*, Liaoyong Wen[1,2,3]*

Affiliations:

[1]Research Center for Industries of the Future (RCIF), School of Engineering, Westlake University, Hangzhou 310024, China.

[2]Zhejiang Key Laboratory of 3D Micro/Nano Fabrication and Characterization, School of Engineering, Westlake University, Hangzhou, Zhejiang 310030, China.

[3]Westlake Institute for Optoelectronics, Fuyang, Hangzhou, Zhejiang 311421, China.

[4]Department of Biomedical Engineering, City University of Hong Kong, Kowloon Tong, Hong Kong, China

[5]Hong Kong Centre for Cerebro-Cardiovascular Health Engineering, Hong Kong Science Park, New Territories, Hong Kong, China.

[6]Institute of Digital Medicine, City University of Hong Kong, Hong Kong, China

[7]Hong Kong Institute for Clean Energy (HKICE), City University of Hong Kong, Hong Kong, China

*Corresponding author. Email: xingeyu@cityu.edu.hk, wenliaoyong@westlake.edu.cn

Contents

1. Supplementary texts and figures

1.1 Fabrication of imprinting moulds

To fabricate Ni nanoimprinting moulds, a silicon master mold featuring a nanohole array (400 nm spacing) in hexagonal and square arrangements was first cleaned in a Piranha solution (H_2O_2/H_2SO_4 = 1:3), followed by rinsing with deionized water[1]. The surface of silicon master was then hydrophobized using 1H,1H,2H,2H-perfluorodecyltrichlorosilane, followed by sputtering a 20 nm Au layer to facilitate Ni electrodeposition. Electrodeposition was carried out with a current density of 10 mA/cm^2 in an electrolyte containing 0.12 M $NiCl_2 \cdot 6H_2O$, 0.12 M $NiSO_4 \cdot 6H_2O$, and 0.5 M H_3BO_3. The Ni nanoimprinting moulds were then obtained by detaching the electrodeposited films from the Si master moulds.

Ni microimprinting moulds with micropyramid arrays were fabricated using a combination of photolithography and chemical etching techniques[2]. Following the same surface fluorination treatment, the silicon master mold was prepared to facilitate the subsequent detaching of the nickel film. Subsequently, nickel electroplating was performed with the same sputtering method and electrolyte composition, but with an increased current density of 15 mA/cm^2.

Microimprinting moulds featuring microrod arrays were fabricated through via photolithography and reactive ion etching (RIE-101iPH). Initially, a wafer was spin-coated with AZ 6124 at 500 rpm for 5 s and then at 3000 rpm for 30 s, followed by baking at 110 ℃ for 90 s. Subsequently, UV exposure (λ = 365 nm, dose = 250 mJ/cm^2) was applied to the wafer using a photomask, and the pattern was developed in AZ MFI 300 solution for 60 s. The developed pattern was etched to a depth of ~2.5 μm using RIE, and the resulting structure was used as a master mould for Ni electrodeposition.

Microimprinting moulds featuring microdome arrays were fabricated by combining thermal reflow and electrodeposition[3]. Initially, a wafer was coated with photoresist AZ 9260, spun at 500 rpm for 5 s and then at 4000 rpm for 30 s, and soft-baked at 110 ℃ for 60 s on a hotplate. A wafer coated with AZ 9260 photoresist underwent UV exposure (dose = 1800 mJ/cm²), then the pattern was developed in AZ MFI 300 solution for 300 s. The microrod arrays formed on the wafer were reshaped into microdomes via thermal reflow at 140 ℃ for 3 minutes. Subsequently, a mixture of polydimethylsiloxane (PDMS) polymer and a curing agent was cast onto the photoresist master mould. After curing, the PDMS polymer was peeled from the resist master mold and treated with 1H,1H,2H,2H-perfluorodecyltrichlorosilane and sputtered with a 20 nm Au layer. Electrodeposition at a current density of 15 mA/cm^2 was conducted, and the Ni microdome mould was obtained by peeling the film from the PDMS template.

1.2 Fabrication of multiscale heterointerfaces

All heterointerfaces were constructed using multiscale anodized aluminum oxide (M-AAO) templates, fabricated via pattern-guided anodization. Initially, high-purity aluminum foil (250 μm thick) was cut into 2×2 cm substrates and sequentially cleaned in acetone, ethanol, and deionized water for 10 minutes each. Subsequently, electropolishing was performed in a 1:9 perchloric acid/ethanol solution for 3 minutes at a current of 0.9 A and voltage of 20 V. Next, the prepared aluminum substrate underwent nanopatterning using a Ni nanoimprinting mould (400 nm spacing), under a pressure of ~14 MPa, followed by microimprinting with a Ni micropyramid mould (20 μm spacing) at ~10 MPa. The multiscale-patterned aluminum substrate was subsequently anodized at 160 V in 0.3 M H_3PO_4 at 5°C for 15 minutes. Pore widening was achieved by immersing the M-AAO template in a 5 wt% phosphoric acid

solution at 30°C for varying durations (30, 60, 90, and 120 minutes), producing M-AAO templates with different pore sizes.

Next, a 100 nm-thick metal layer (Ag, Au, Cu, Pt) was deposited onto the M-AAO template surface via sputtering. The metal-coated M-AAO template was then covered with PDMS mixture (10:1 ratio of polymer to curing agent) and spin-coated at 300 rpm for 30 s, followed by 500 rpm for 30 s. To eliminate bubbles and ensure the PDMS mixture penetrated the nanopores, the sample was placed in a vacuum oven for 15 minutes. Curing was performed at 70°C for 30 minutes on a hotplate. Finally, the non-anodized aluminum substrate and M-AAO template were dissolved in a $CuCl_2 \cdot 2H_2O$/HCl solution (8.5 g in 500 ml of 15 wt% HCl) and 0.3 M H_3PO_4 solution, respectively, to obtain the multiscale heterointerface on the PDMS substrate with integrated functional materials. Different multiscale heterointerfaces with various polymer substrates can be achieved by simply altering the precursor of the polymer solution.

For different Au/PDMS multiscale heterointerfaces, plane structures were fabricated by directly sputtering metal onto the unpatterned PDMS substrate. Nanostructured samples were fabricated via nanoimprinting and anodization, employing the same anodization voltage, duration, and pore-widening conditions as previously described. Microstructured samples were fabricated by imprinting a Ni film with micropyramid arrays onto the aluminum surface, transferring the pattern to PDMS, and subsequently applying metal sputtering.

1.3 Mechanical robustness test of multiscale heterointerface

The mechanical stability of the multiscale heterointerface in strain sensors was evaluated through ultrasonic testing. Au/PDMS multiscale heterointerface samples were placed on a glass

slide, submerged in water to maintain consistent depth, and subjected to ultrasound. The conductivity of each sample was then assessed by measuring square resistance.

Tape-peeling tests were performed to assess the adhesion stability of the multiscale heterointerface. Gold, serving as the conductive circuit, was sputtered onto a polyimide (PI) flexible substrate without an adhesive layer, using a mask for circuit patterning. The mechanical anchoring strategy enabled stable connections between the conductive PI film and the LED light-emitting circuit, where current variations corresponded to changes in LED power. A 10 μm thick, 15 mm wide polyimide tape was used for the peel-off tests, applying pressure via a 500 g cylindrical block as a roller.

The abrasion test was conducted to further evaluate the mechanical stability of the multiscale heterointerface. A cylindrical object (1.5 cm in diameter) holding 3000-grit sandpaper was applied under fixed pressure. A polyimide (PI) film with a gold conductive circuit was mounted on a sliding rail for abrasion testing, which involved back-and-forth motion. LED lamp luminous power was monitored using a Keighley 2450, providing feedback during the test.

1.4 Fabrication and sensing performance test of the strain sensor

The strain sensor was fabricated using the Au/PDMS multiscale heterointerfaces. The Au/PDMS heterointerface was dried in an oven at 60 ℃ for 10 minutes to ensure a fully dry surface. Silver paste was then applied between the sensing layer and copper tapes to ensure optimal electrical contact.

To evaluate the sensing performance of the strain sensors, a motorized test system equipped with a force gauge (Mark 10 ESM303) was employed to apply strain. Resistance profiles were

monitored using the Keighley 2450. The tensile response of the strain sensor was tested at a strain rate of 10 mm/min.

1.5 Robustness test of strain sensor

To evaluate the mechanical and electrical stability of the strain sensor under various harsh environmental conditions, a series of tests were conducted, including long-term cyclic testing, normal pressure decoupling, hydrophobicity and high-temperature stability assessments. For the cyclic stability, a strain sensor (15mm×10mm) with an Au/PDMS heterointerface, incorporating different structures, was assessed under a 15% strain range during loading. The tensile response was measured at a strain rate of 100 mm/min.

The sensor's ability to decouple normal pressure was assessed using a strain sensor (15 mm × 10 mm) with an Au/PDMS multiscale heterointerface. The sensor was mounted on a biaxial horizontal displacement stage, with strain applied by sliding the stage. Normal pressures were exerted using a force gauge (Mark 10 ESM303). The sensor's performance in real-world static and dynamic environments was also evaluated by placing it on the ground while a car weighing approximately 2730 kg drove over it, both forward and in reverse. Data were transmitted via Bluetooth from the sensor, which was connected to a data acquisition module.

The sensor's waterproof properties and the stability of its functional materials and heterointerface at high temperatures were further tested. A serpentine circuit, designed via a mask, was employed to detect pulse signals and assess the sensor's resistance to water impact, with water flowing at 4 m/s from a faucet. The thermodynamic stability was evaluated by subjecting the sensor to 10% strain while it was fixed on a hot stage, with the temperature

147 gradually increased. Surface temperature changes were monitored using an infrared thermal
148 imager (Guide PC230).

149 **1.6 3D tactile perception of robots using strain sensor**

150 The fabrication of strain sensors follows the same process as previous devices, with the
151 exception of using a metal mask during the PVD process. A macroscopic optimized pattern
152 was achieved through mechanical simulation. The nanostructure incorporates hexagonal
153 nanoholes with a spacing of 400 nm, while the microstructure features 10 μm pyramids with a
154 spacing of 10 μm. This nano-to-macro pattern design allows for precise adjustment of the high-
155 sensitivity sensing range to specific requirements. Large-area patterns were fabricated using a
156 self-designed mechanical imprint stepper.

157 For 3D tactile testing, the sensor was positioned on the upper surface of a 3D-printed
158 cantilever probe measuring 15 × 50 mm with a thickness of 300 μm. The cantilever probe was
159 mounted on a linear motor to ensure consistent contact between the probe and the testing
160 material. The testing patterns and materials were secured by a balance, and the force exerted
161 by the probe on the balance was maintained at approximately 3 mN to ensure consistency
162 across each test.

163 **1.7 Structures and materials characterization**

164 SEM images and energy-dispersive X-ray spectroscopy (EDS) analysis were performed
165 using a field-emission scanning electron microscope (FE-SEM, ZEISS, Gemini500). The
166 contact angle measurements were conducted with a contact angle tester (Data Physics, OCA
167 25). Resistance profiles were monitored using a Keighley 2450 source meter, while square
168 resistance was measured using a four-probe meter (ST2258C, Suzhou Jingge Electronics Co.,

Ltd). Optical photographs of the textures were acquired by an optical microscope (LW750LJT, Shanghai Cewei Optoelectronic Technology Co., Ltd).

1.8 Solid mechanical simulations

Strain, stress distribution, and deformation were analyzed using COMSOL Multiphysics 5.6 software, employing a hyperelastic model based on the Neo-Hookean constitutive model. A simplified two-dimensional representation of the micropatterned Au/PDMS model was designed using CAD software and imported into COMSOL Multiphysics for analysis. The Young's modulus and Poisson's ratio of the Au film were set to 70 GPa and 0.44, respectively, while the Young's modulus of the PDMS substrate was set to 750 kPa. The hexagonal nanopore arrangement was modeled with a fixed period of 400 nm, and nanopore diameters of 100 nm, 200 nm and 300 nm. The square micropyramid arrangement was defined with a 1.5 μm period, and spacing of 1.5 μm, 2.25 μm, and 3 μm. In the numerical analysis, one end of the model was fixed, while a defined tensile strain was applied to the opposite end.

1.9 Statistical analysis

All statistical analyses were conducted using SPSS 26.0 (IBM, Armonk, NY, USA). Crack morphologies at specific magnifications were captured via SEM and subsequently analyzed using ImageJ software (NIH, Bethesda, MD, USA). Quantitative data were expressed as mean ± standard deviation (s.d.).

2. Supplementary Note

2.1 Electromechanical analysis of the strain sensor

We developed a simplified crack model, where the film is segmented into "effective cracking paths" that extend laterally across the entire film. Under uniaxial tensile loading, stress

concentrations at the cracking sites lead to these regions bearing the majority of the applied strain.

The relationship between the average crack width (D), the applied strain (ε), and the line density of effective cracking paths (N) is described by the equation:

$$D = \frac{\alpha\varepsilon}{N} \tag{1}$$

The total resistance of the system consists of two contributions: the crack zone and the metal zone within an effective cracking path. The resistance from the crack zone is modeled as a strain-dependent tunneling effect, while the metal zone contributes based on its geometrical and material properties.

For the crack zone, the resistance is expressed as[4]:

$$R_{crack} = \frac{h^2 D}{Ae^2\sqrt{2m\phi}} \exp\left(\frac{4\pi D}{h}\sqrt{2m\phi}\right) = B_1 \frac{\varepsilon}{N} e^{B_2 \frac{\varepsilon}{N}} \tag{2}$$

For the metal zone, the resistance is given by:

$$R_{metal} = \frac{\rho d}{tMW} = \frac{B_3 \varepsilon}{NG} \tag{3}$$

Here, h is Planck's constant, D is the average crack width, Φ denotes the energy barrier height, and A is the cross-sectional area of the tunnel conducting zone. The parameters m and e denote the electron's mass and charge, respectively. Coefficients B_1 and B_2 incorporate these quantities. Additionally, ρ and t represent the resistivity and thickness of the metal film, respectively, while W is the total width of the metal film. B_3 is another integrated coefficient. The variable G, ranging from 0 to 1, describes the degree of electrical conduction in the presence of cracks. G=0 indicates complete electrical isolation due to through cracks, while G=1 signifies a fully conductive metal film without cracks.

By combining the aforementioned equations, the strain-dependent resistance changes for a film with N^*n_0 effective cracking paths can be described by the following equation:

$$\Delta R = \sum_{i=1}^{Nn_0} \frac{1}{\frac{1}{R_{cracki}}+\frac{1}{R_{metali}}} = \frac{c_1 c_3 n_0 \varepsilon e^{\frac{c_2\varepsilon}{N}}}{G c_1 e^{\frac{c_2\varepsilon}{N}}+c_3} \quad (4)$$

Where n_0 represents the number of effective cracking paths, and N is the line density of effective cracking paths. As depicted in the equation, the strain-dependent resistance change of the metal film is primarily governed by two key parameters, N (the crack density) and G (the degree of electrical continuity). The three distinct crack behaviors illustrated in Figure 3**a** and **g** are characterized by variations in N and G. Notably, the presence of cut-through cracks in the three crack modes indicates a feature where G=0. The strain-dependent resistance change follows an exponential relationship, further influenced by N:

$$\Delta R = c_1 n_0 \varepsilon e^{\frac{c_2\varepsilon}{N}} \quad (5)$$

From experimental results, we observe that the effective crack density N follows this order:

$$N_{\text{cross}} > N_{\text{wave}} > N_{\text{parallel-1}} > N_{\text{parallel-2}} \quad (6)$$

Consequently, the resistance change exhibits the inverse trend:

$$\Delta R_{cross} < \Delta R_{wave} < \Delta R_{\text{parallel-1}} < \Delta R_{\text{parallel-2}} \quad (7)$$

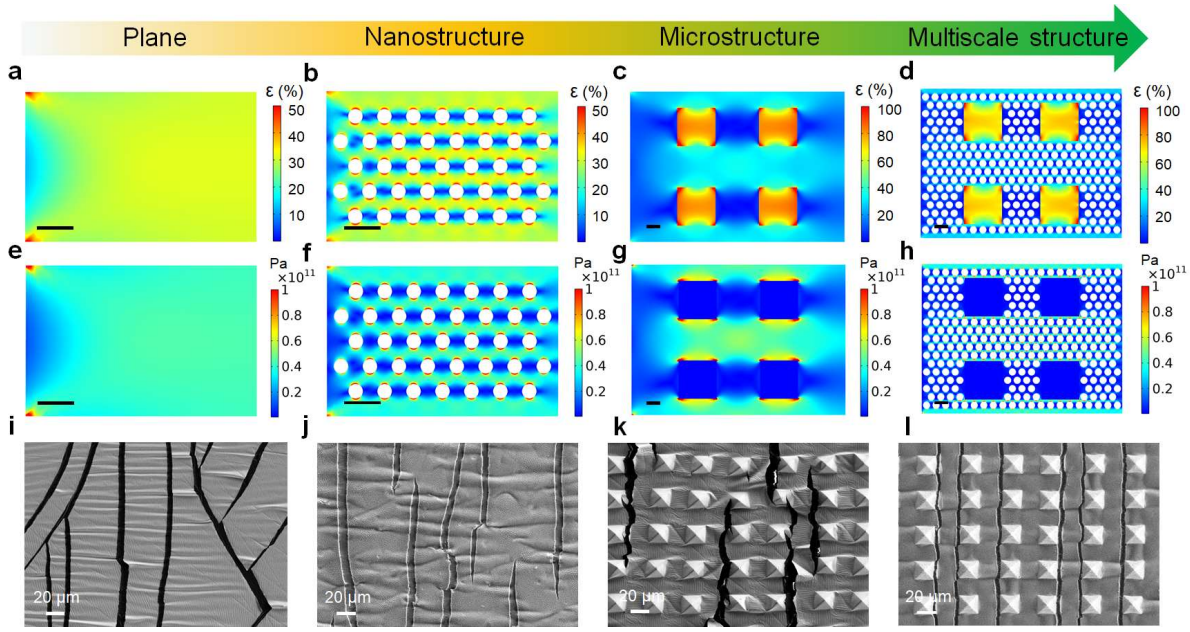

Supplementary Fig. 1. Finite Element Analysis (FEA) of stress distributions and corresponding SEM images under uniaxial tension for different Au/PDMS heterointerfaces. (a-d) Simulated strain distributions for the plane, nanostructured, microstructured, and multiscale interfaces, respectively. The scale bar is 500 nm. **(e-h)** Simulated stress distributions for the plane, nanostructured, microstructured, and multiscale interfaces, respectively. The scale bar is 500 nm. **(i-l)** SEM images depicting crack propagation in the different Au/PDMS heterointerfaces under uniaxial tension.

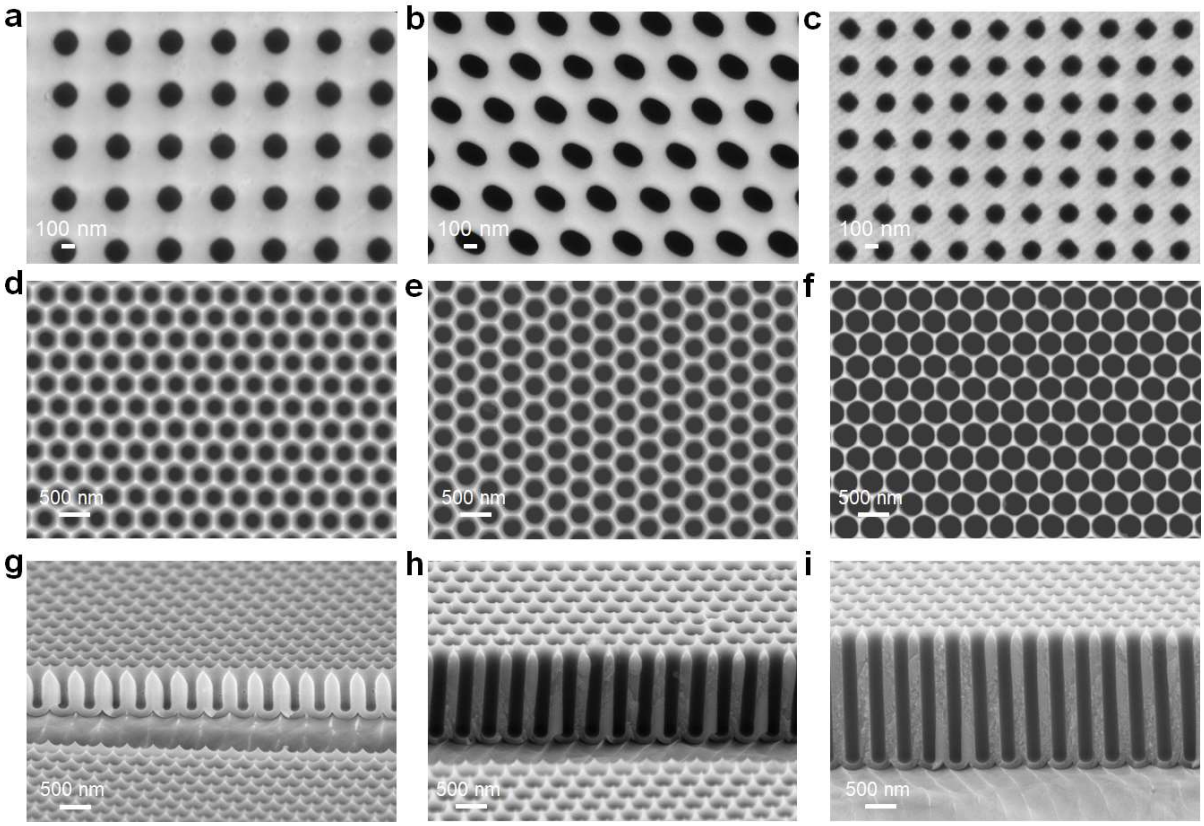

Supplementary Fig. 2. Tunable nanofeatures of M-AAO templates. (a-c) Morphology, arrangement, and periodicity of nanostructures adjusted via nanoimprinting. **(d-f)** Nanohole sizes modified through controlled wet etching. **(g-i)** Aspect ratios tailored by varying the anodization time.

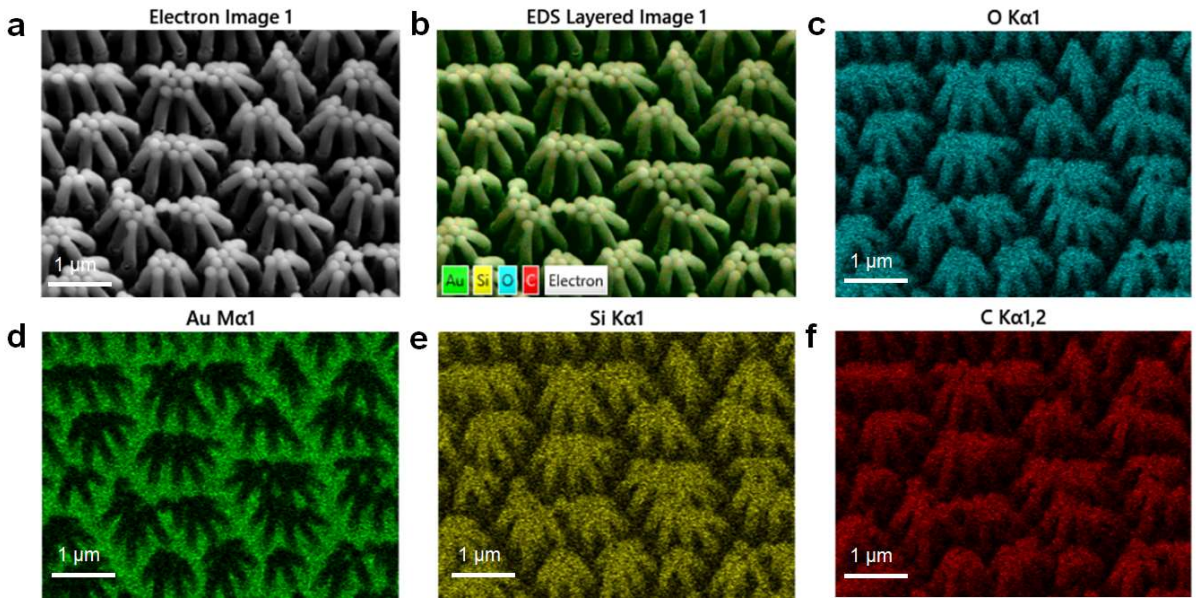

Supplementary Fig. 3. Characteristics of the Au/PDMS multiscale heterointerface. a) SEM image and the corresponding EDS maps: elemental distribution map of the mixture (**b**), oxygen (**c**), gold (**d**), silicon (**e**), and carbon (**f**).

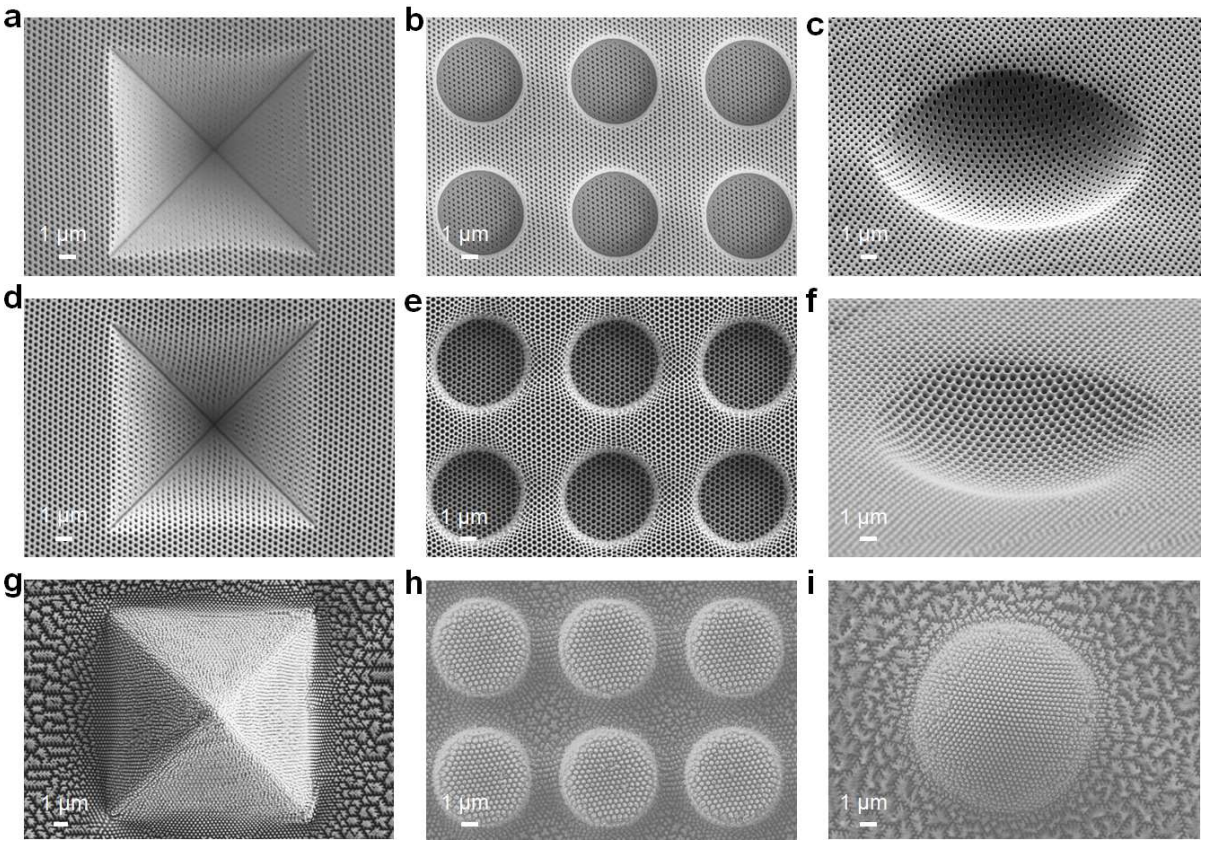

Supplementary Fig. 4. Microfeatures adjustment of the M-AAO templates and corresponding multiscale heterointerface. (a-c) Morphological adjustments of the microstructures via microimprinting. **(d-f)** Anodization of the nano-micro-patterned aluminum foils. **(g-i)** Formation of Au/PDMS multiscale heterointerfaces with distinct microstructures, including micropyramids, micropillars, and microdomes.

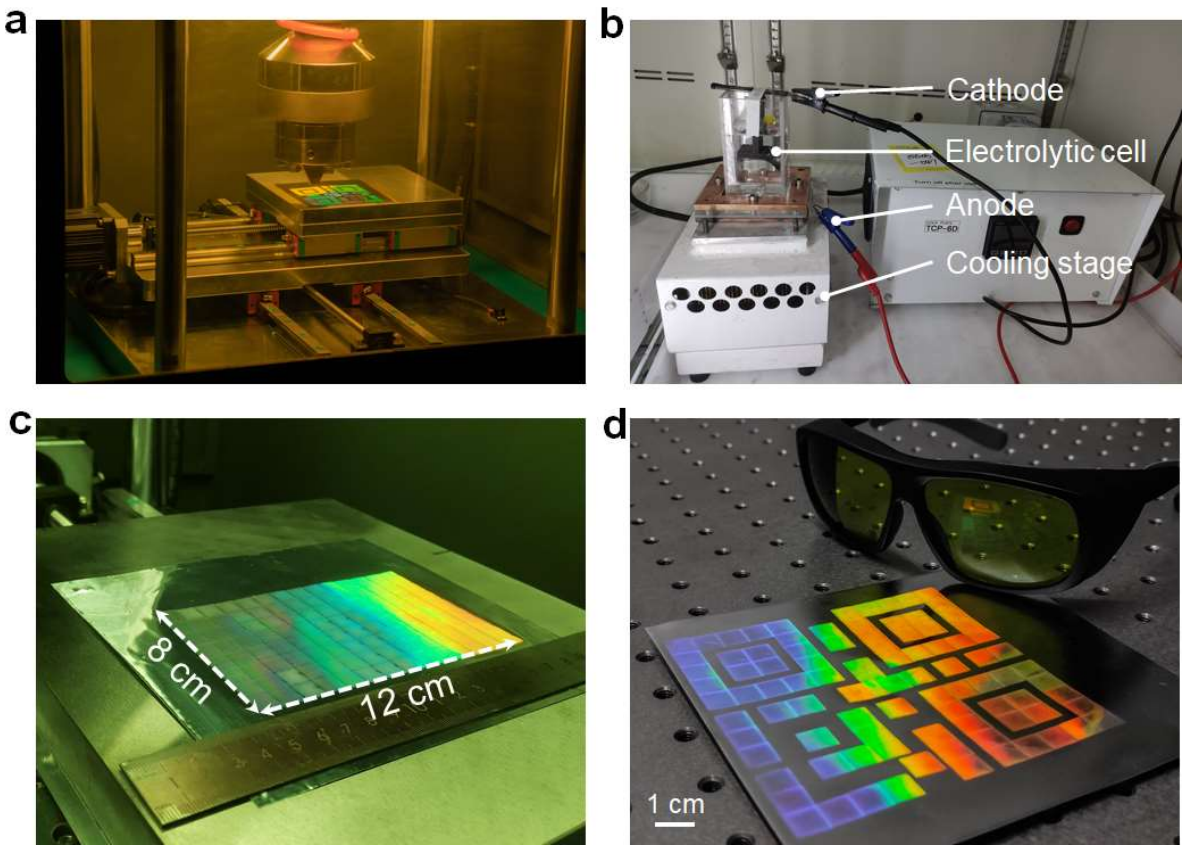

Supplementary Fig. 5. Self-designed and assembled equipment for imprinting and anodization. a) The automatic imprinting system comprises an imprinted head, substrate, and an XY displacement stage. **b)** Electrolytic cell positioned on a cooling stage for heat dissipation during anodization. The anodization process was carried out in a constant-temperature refrigerator, maintained between 2–5 °C. **c)** Representatively large-area imprinted aluminum foil. **d)** Customizable imprinted pattern of the aluminum foil.

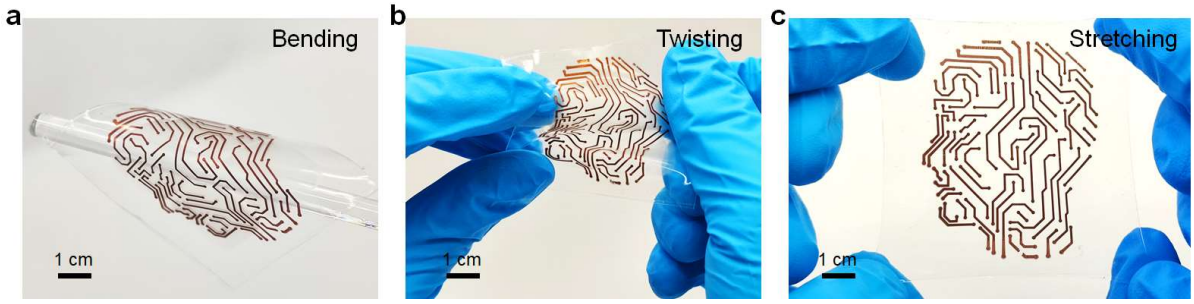

Supplementary Fig. 6. Macropattern adjustment of the Au/PDMS multiscale heterointerface using a shade mask during Au deposition. (a-c) Representative images of the Au/PDMS multiscale heterointerface subjected to complex deformation conditions.

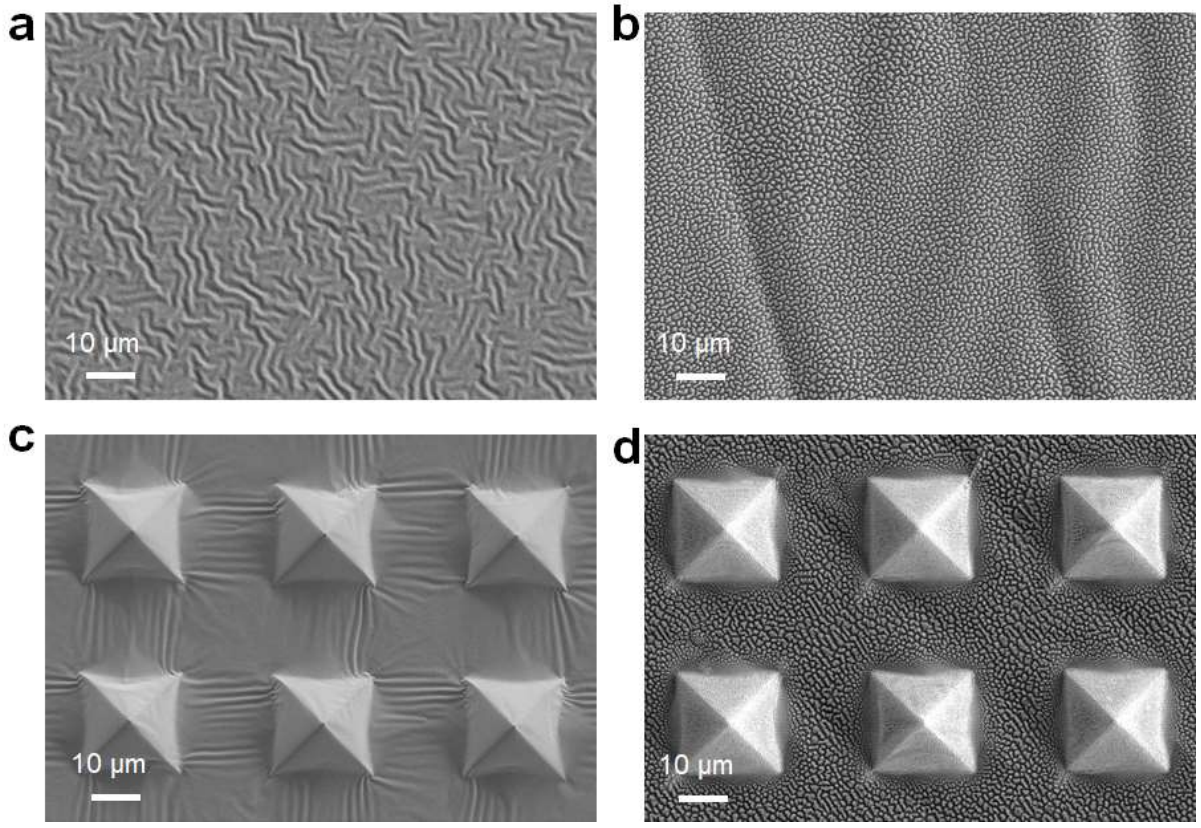

Supplementary Fig. 7. SEM images of different Au/PDMS heterointerfaces. (a-d) Mechanical heterointerfaces featuring a planar surface, nanofibers, micropyramids, and a multiscale structure.

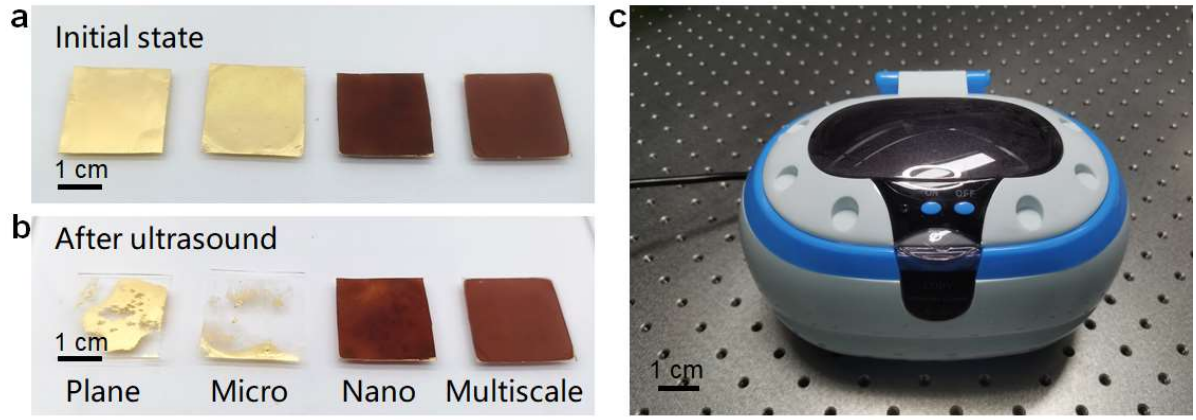

Supplementary Fig. 8. Photographs of different Au/PDMS heterointerfaces subjected to ultrasound exposure. a) Initial state of the Au/PDMS heterointerfaces. **b)** Au/PDMS heterointerfaces after 9 seconds of ultrasound treatment. **c)** Photograph of the ultrasound machine used in the experiment.

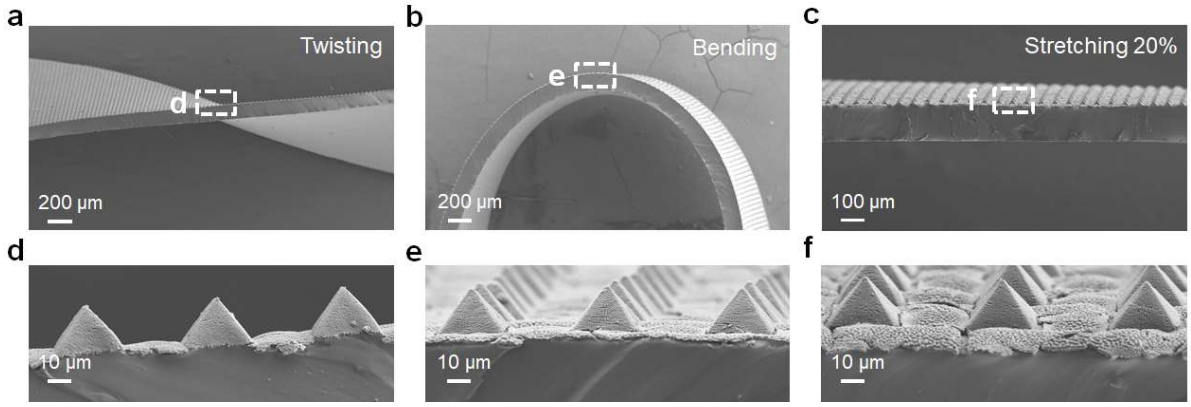

Supplementary Fig. 9. Au/PDMS multiscale heterointerfaces under various deformation conditions. (a-f) In-situ SEM images illustrating the behavior of Au/PDMS multiscale heterointerfaces subjected to twisting, bending, and stretching conditions.

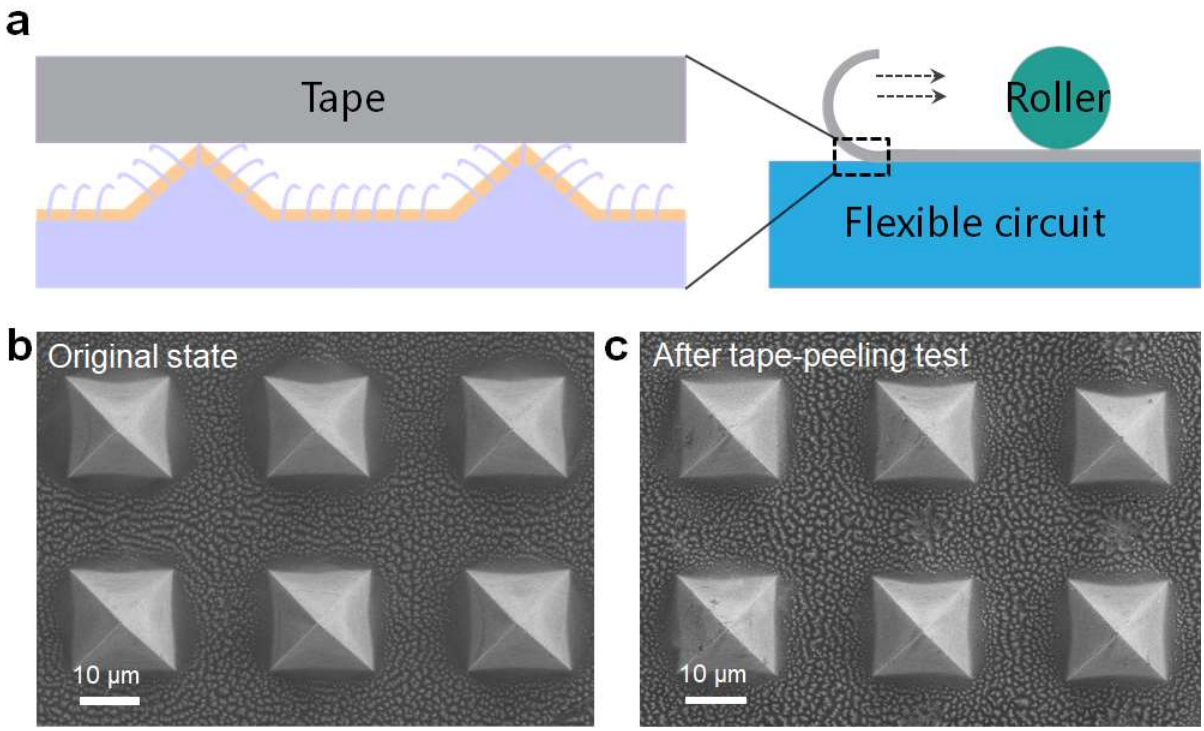

Supplementary Fig. 10. Schematic illustration and SEM images of the Au/polyimide multiscale heterointerface. a) Schematic illustration of the tape-peeling test, where tape is applied under uniform pressure using a roller. **b), c)** SEM images showing the original state and the post-tape-peeling condition of the Au/polyimide multiscale heterointerface.

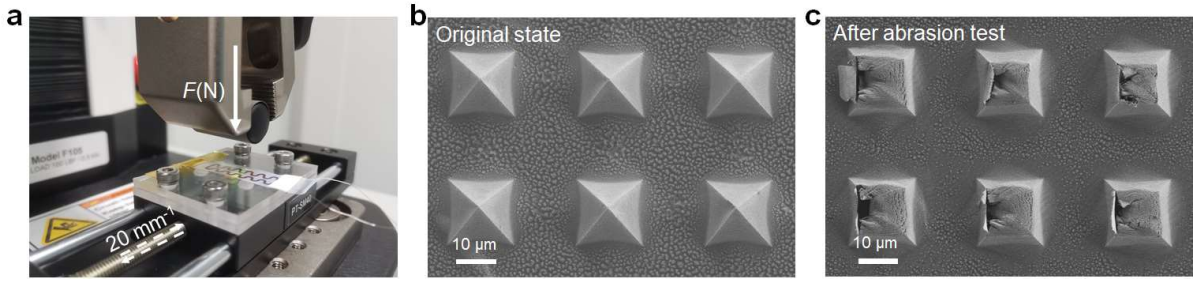

Supplementary Fig. 11. Abrasion test of the Au/polyimide multiscale heterointerface. a) Photograph of the abrasion setup. **b), c)** SEM images depicting the original state and the condition of the Au/polyimide multiscale heterointerface after the abrasion test.

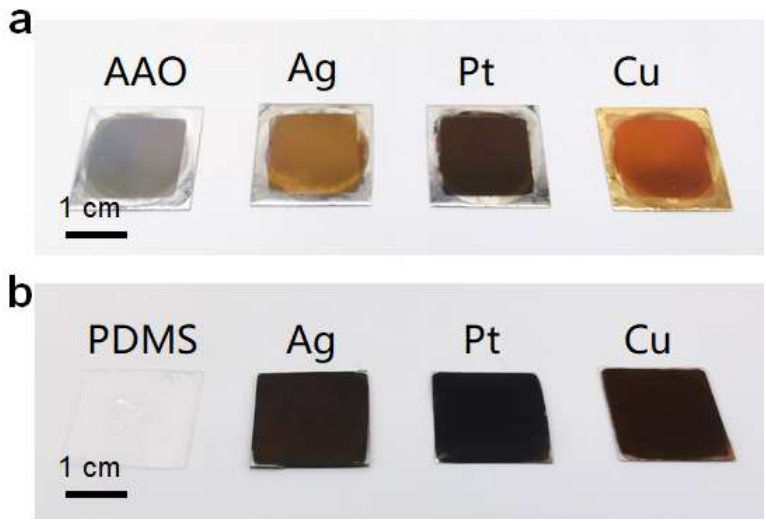

294

295 **Supplementary Fig. 12.** Photographs of different metals on M-AAO templates **(a)** and PDMS

296 substrates following the dissolution of the M-AAO templates **(b)**.

297

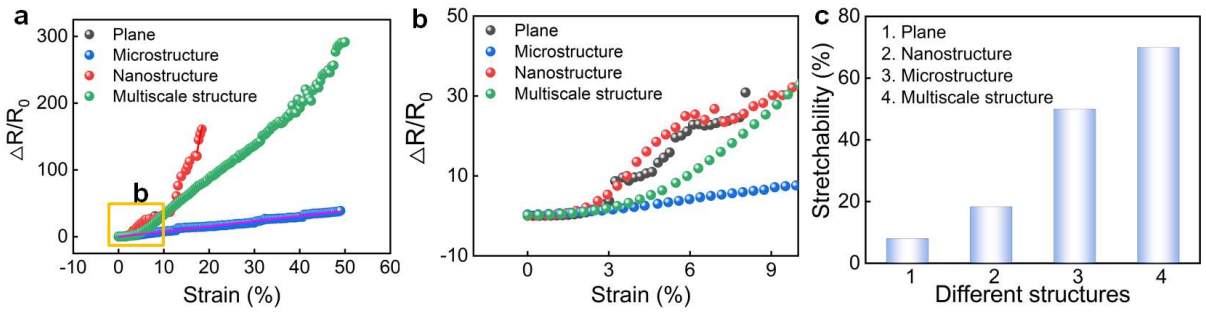

Supplementary Fig. 13. Resistance response of strain sensors with different heterointerfaces. a), **b)** Relative resistance changes of strain sensors under different strains and enlarged details**. c)** Stretchability of strain sensors featuring different structures.

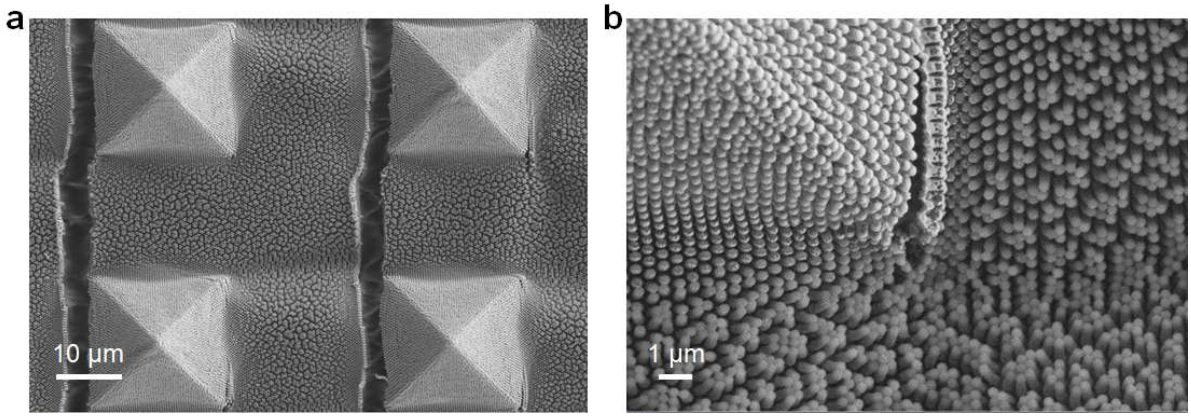

Supplementary Fig. 14. SEM images of the strain sensor with Au/PDMS multiscale heterointerface during stretching. The images illustrate the parallel arrangement and propagation of cracks, with initial cracks originating in the stress concentration areas at the base of the micropyramids, consistent with the FEA results.

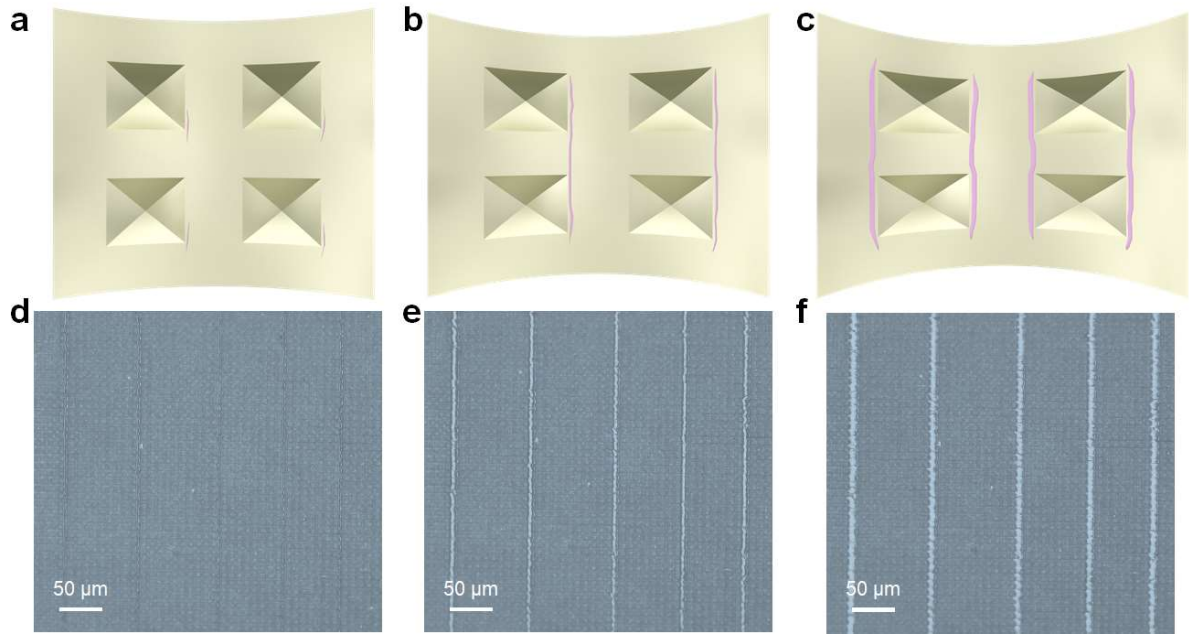

Supplementary Fig. 15. Schematic illustration and photographs of the strain sensor under stretching. The photographs display the morphological evolution of the multiscale heterointerface-based strain sensor at 0%, 25%, and 50% strain. As strain increases, the cracks at the heterointerface expand in parallel and the crack width gradually increases.

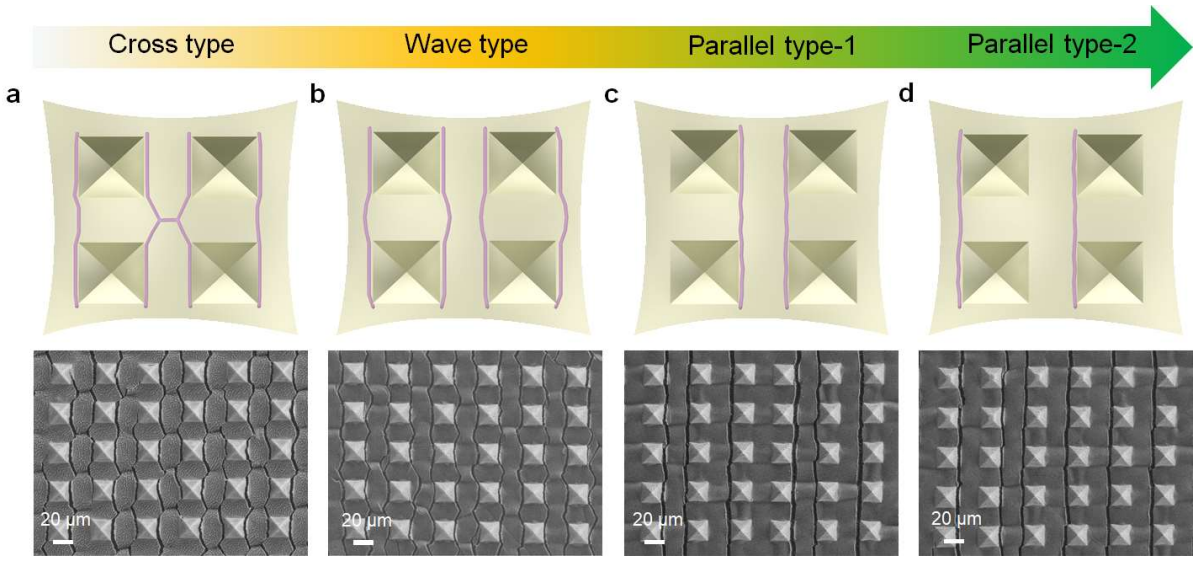

Supplementary Fig. 16. Schematic illustration and SEM images of strain sensors with various multiscale heterointerfaces. This figure showcases crack propagation patterns of multiscale heterointerfaces with different nanofiber sizes under uniaxial tension, including cross-type **(a)**, wave type **(b)**, and parallel types **(c** and **d)**.

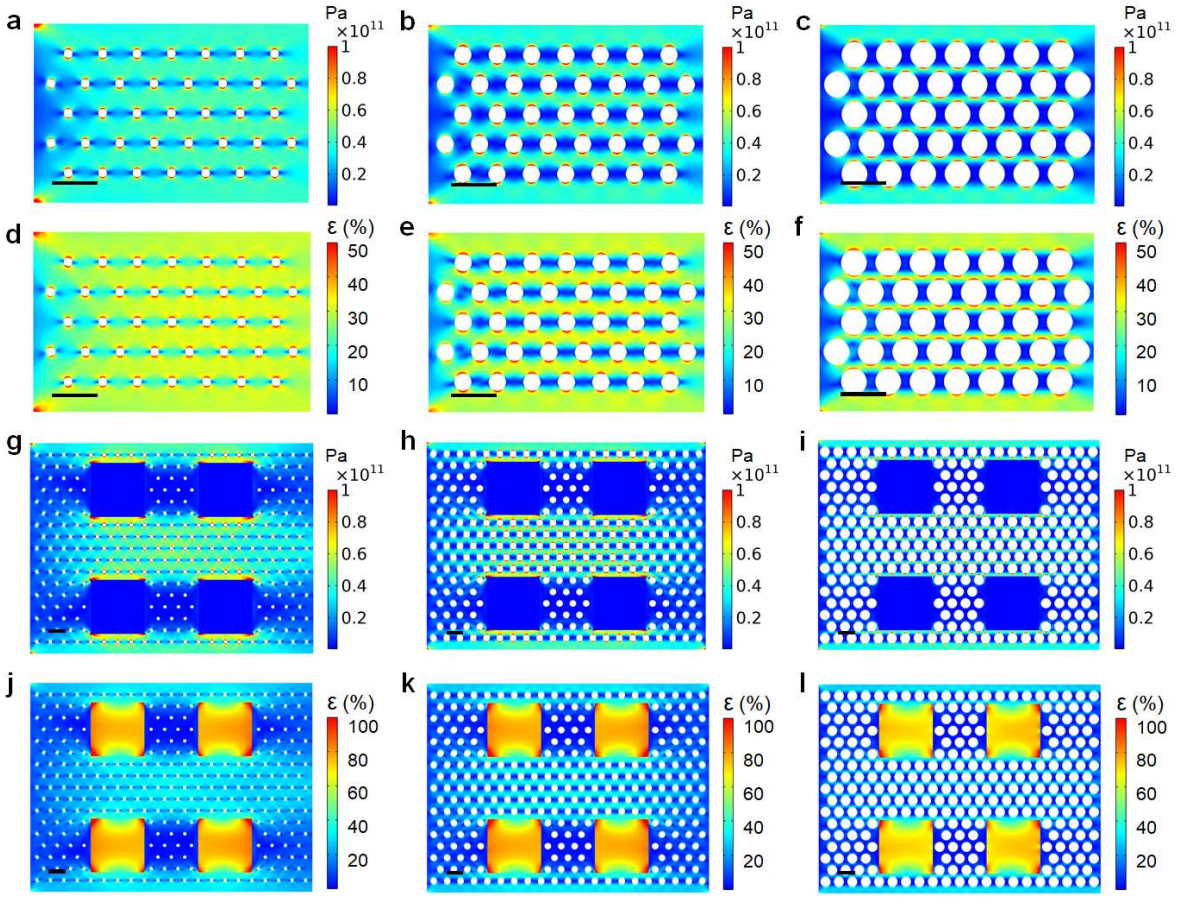

Supplementary Fig. 17. FEA simulated stress and strain distribution for multiscale heterointerfaces with varying nanofiber sizes under uniaxial tension. (a-c) and **(g-j)** display the stress distribution of multiscale heterointerfaces with different nanofiber sizes. The scale bar is 500 nm. **(d-e)** and **(j-l)** illustrate the strain distribution for the multiscale heterointerfaces with different nanofiber sizes. The scale bar is 500 nm.

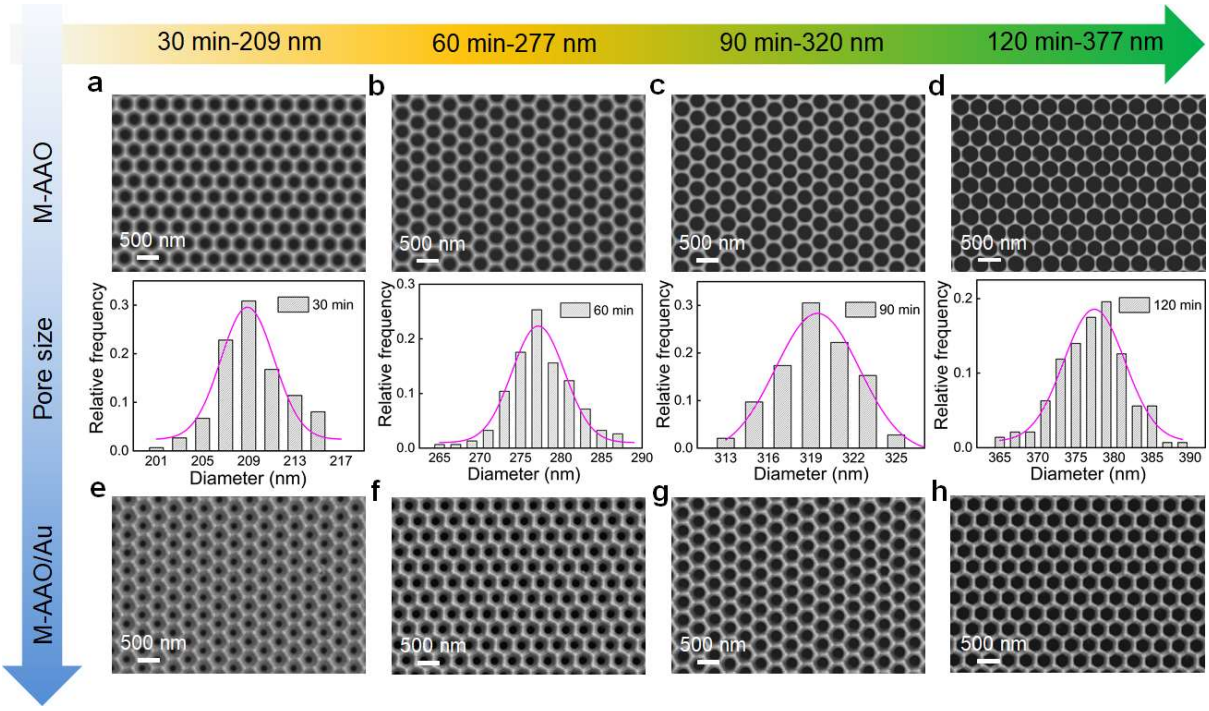

328

329 **Supplementary Fig. 18. Nanohole size adjustment of the M-AAO templates.** Top-down

330 SEM images of the M-AAO templates after different durations of wet etching in 5 wt% H_3PO_4

331 at 30 ℃**: (a)**, 30 min; **(b)**, 60 min; **(c)**, 90 min; **(d)**, 120 min. **(e-f)** Corresponding M-AAO

332 templates following Au deposition.

333

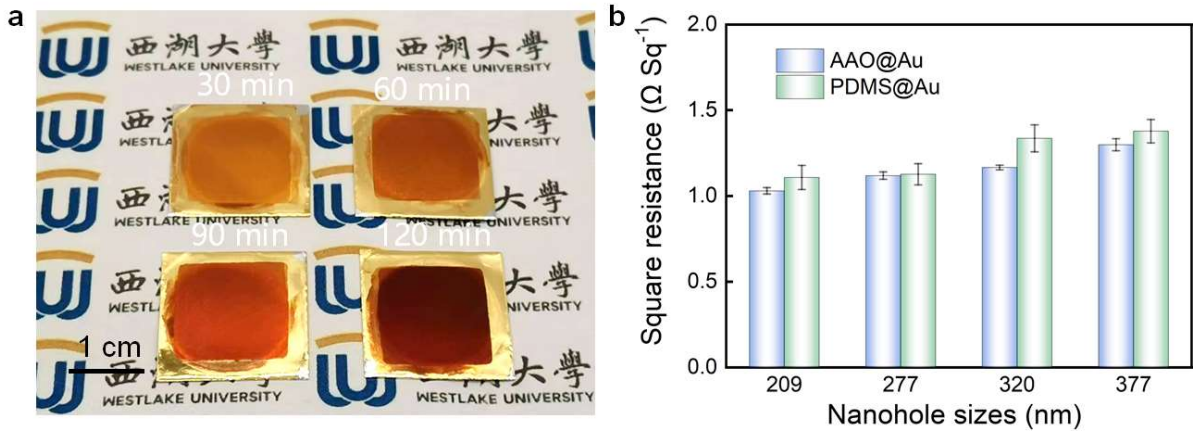

Supplementary Fig. 19. Photograph and square resistance value of M-AAO templates with gold. a) Photograph of the multiscale patterns on an aluminum substrate. **b)** Square resistance of M-AAO templates and PDMS substrate with gold. The results show that the square resistance of the multiscale heterointerface is almost without change before and after gold transfer (n=5). Data points and error bars show the mean ± s.d.

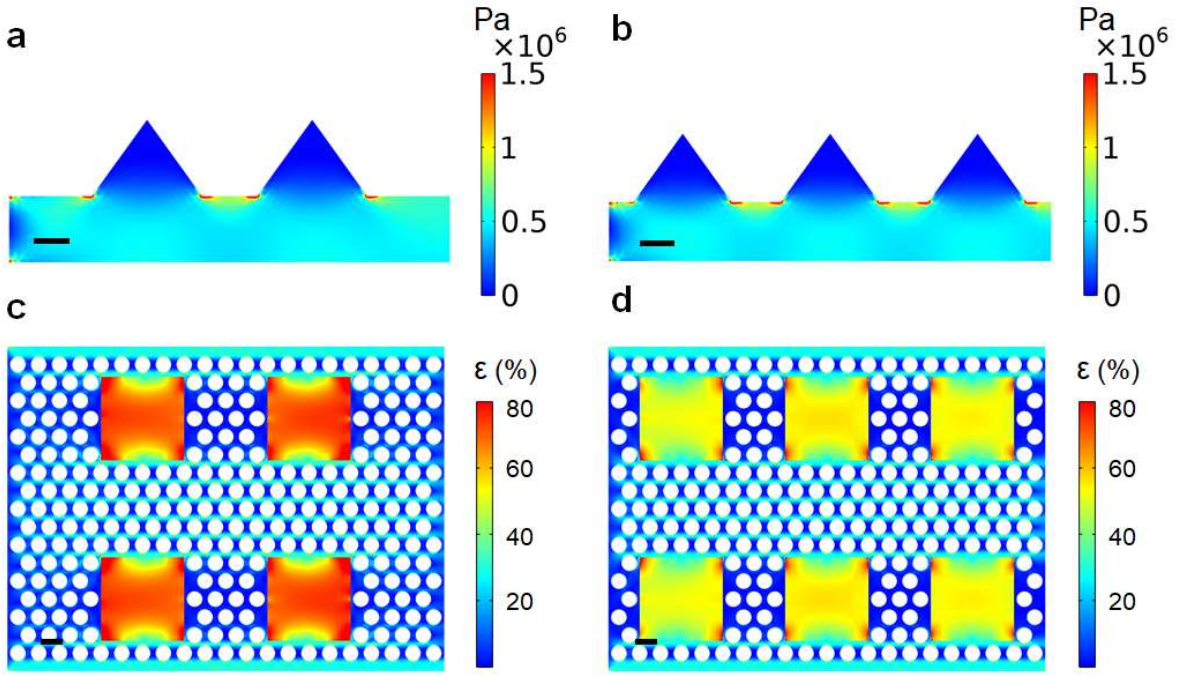

Supplementary Fig. 20. FEA simulated stress and strain distributions with different micropyramids densities under uniaxial tension. (a, b) Stress distributions of the Au/PDMS multiscale heterointerfaces at different micropyramid densities. **(c, d)** Strain distributions corresponding to the same conditions. Scale bar: 10 μm for **(a, b)** and 500 nm for **(c, d)**.

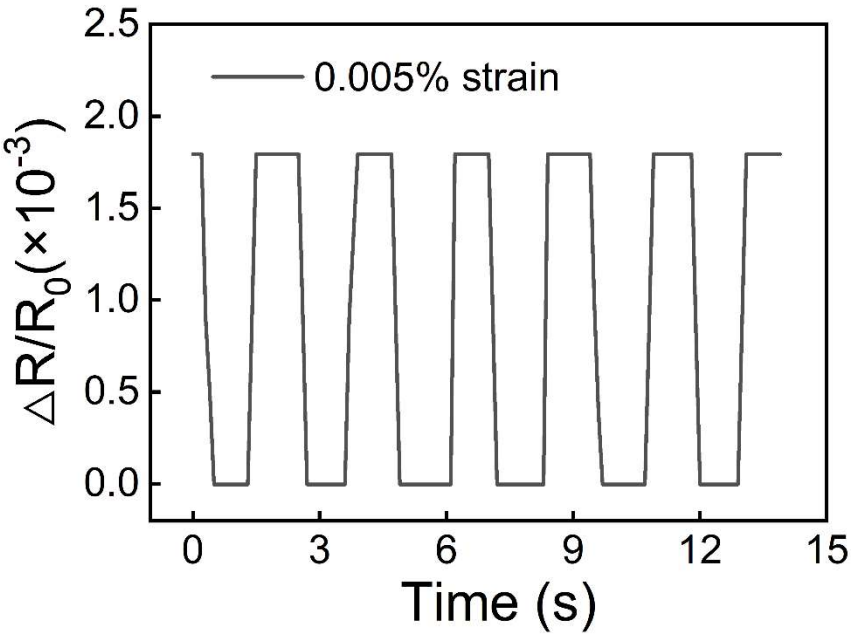

Supplementary Fig. 21. Detection capability of the strain sensor for extremely subtle strains. The sensor's responsiveness to minimal strain variations demonstrates its high sensitivity in strain detection.

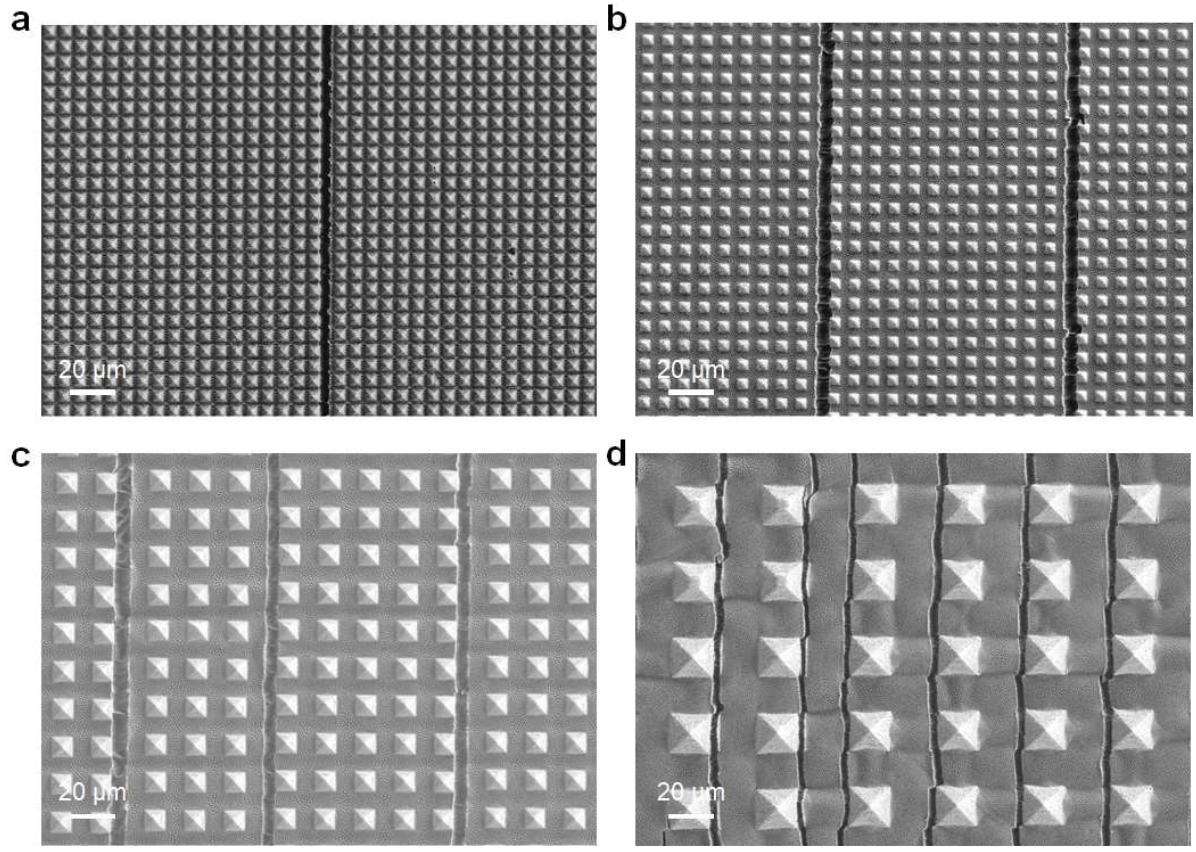

Supplementary Fig. 22. SEM images of multiscale heterointerfaces with different micropyramids densities under uniaxial tension. (a-d) The images show micropyramid arrangements with distances of 2.5 μm, 5 μm, 10 μm, and 20 μm, respectively.

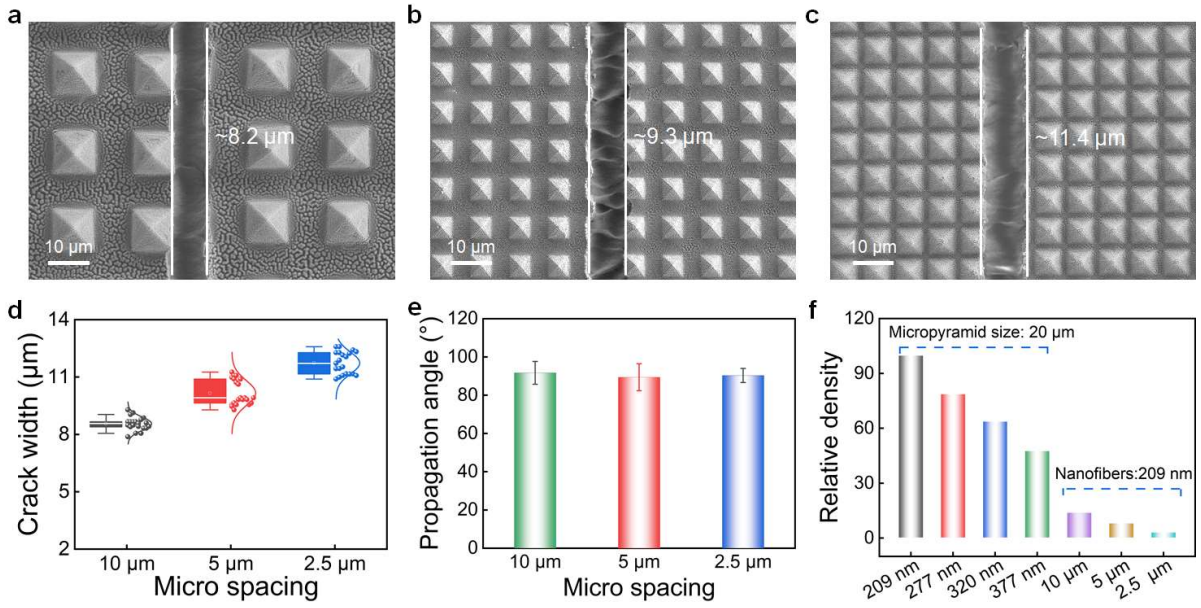

357

358 **Supplementary Fig. 23. Statistical analysis of crack width, propagation angle, and**
359 **relative crack density in multiscale heterointerfaces with different micropyramid**
360 **spacings under 10% strain. (a-c)** SEM images of multiscale heterointerfaces with the same
361 nanofiber sizes but different micropyramid spacings. **d)** Changing of crack widths with the
362 different micropyramid spacings. **e)** Changing of crack propagation angles with the different
363 micropyramid spacings (n=20). **f)** Normalized crack densities as a function of the structural
364 features of the multiscale heterointerface. In **(d)** and **(e)**, data points and error bars show the
365 mean ± s.d.

366

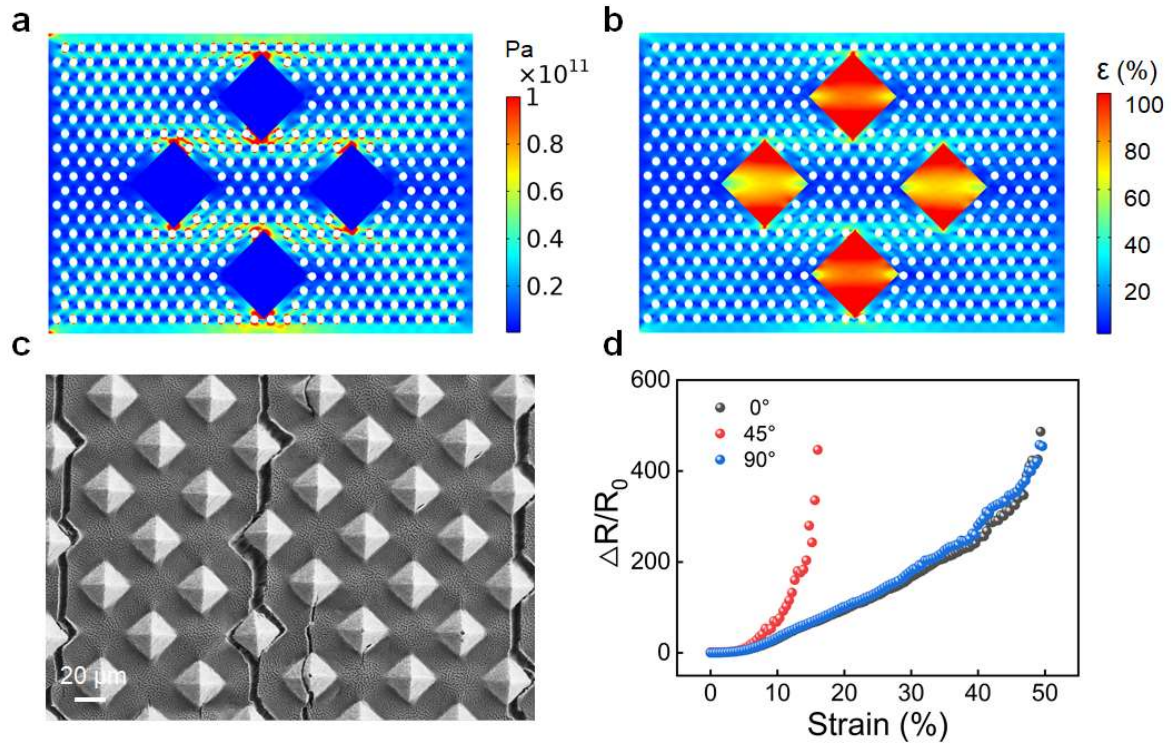

Supplementary Fig. 24. Adjustment of crack propagation mode and density with microimprinting angles. a), b) FEA simulated stress and strain distributions of the multiscale heterointerface featuring rotated micropyramids. **c)** SEM images of heterointerface with rotated micropyramids. **d)** Sensing performance of the strain sensor with different rotated angles.

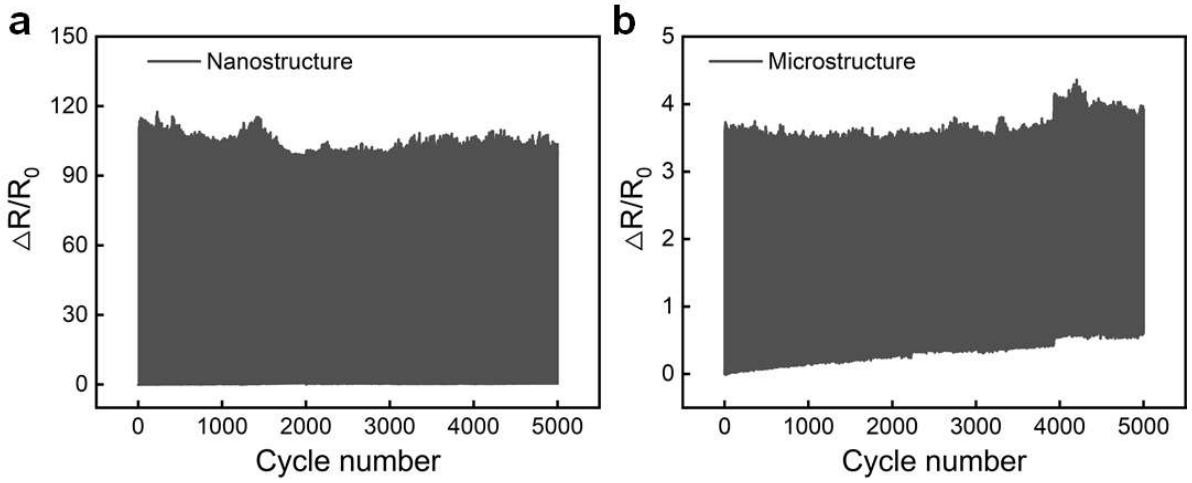

374

375 **Supplementary Fig. 25. Sensing profiles of the strain sensors with nanofibers and**

376 **micropyramids under cyclic loading. a), b)** The electrical signals of both strain sensors

377 exhibit significant drifts after 5000 loading cycles.

378

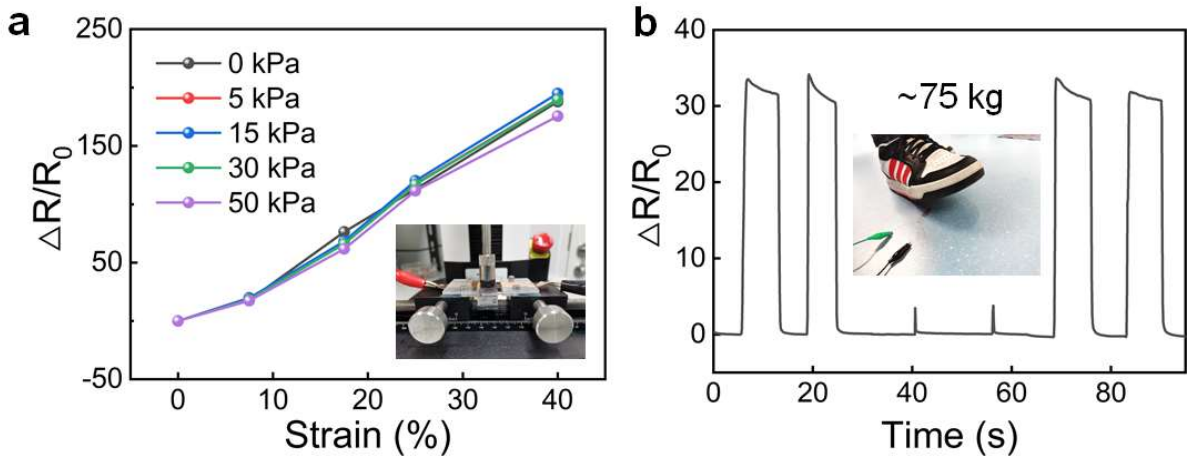

Supplementary Fig. 26. Mechanical decoupling of the strain sensor under normal pressure. a) Relative resistance variation of the strain sensor under different normal pressures. **b)** Demonstration of the normal pressure resistance of the strain sensor to excessive impacts from working of a man weighing 75 kg.

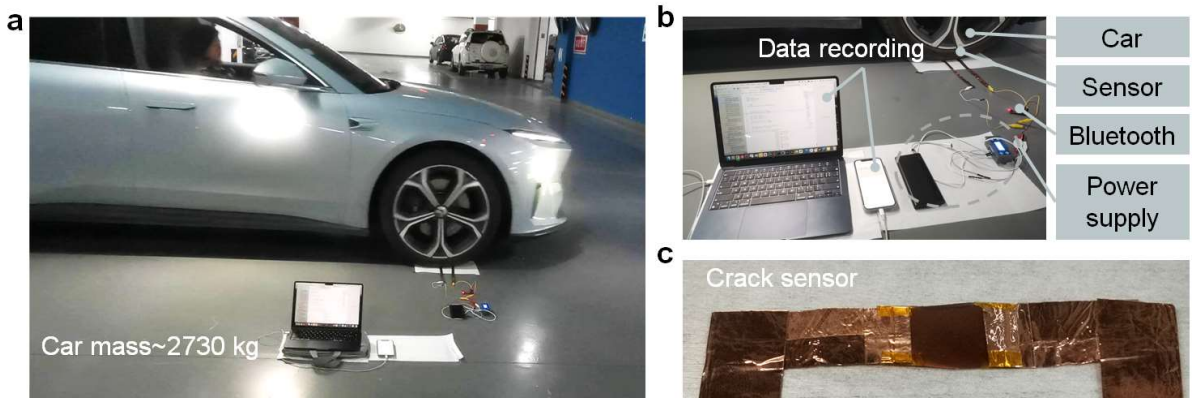

Supplementary Fig. 27. Resilience of strain sensor under extreme loads. a) and **b)** Photographs of the testing setup, which consists of a strain sensor, a data acquisition module, and a Bluetooth transmitter for relaying test data to a computer. The sensor is placed on the ground while a car is driven and reversed over it. **c)** Photograph image of the strain sensor after testing.

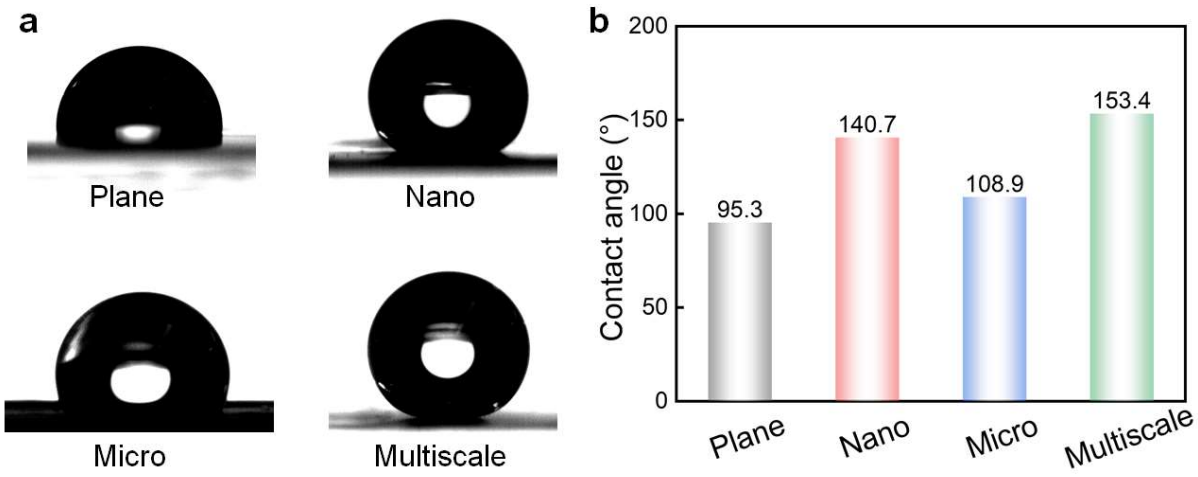

392

393 **Supplementary Fig. 28. Contact angle measurements of the strain sensor with different**

394 **structures.** The results show that the multiscale structure exhibits a superhydrophobic interface

395 with a contact angle of 153.4°.

396

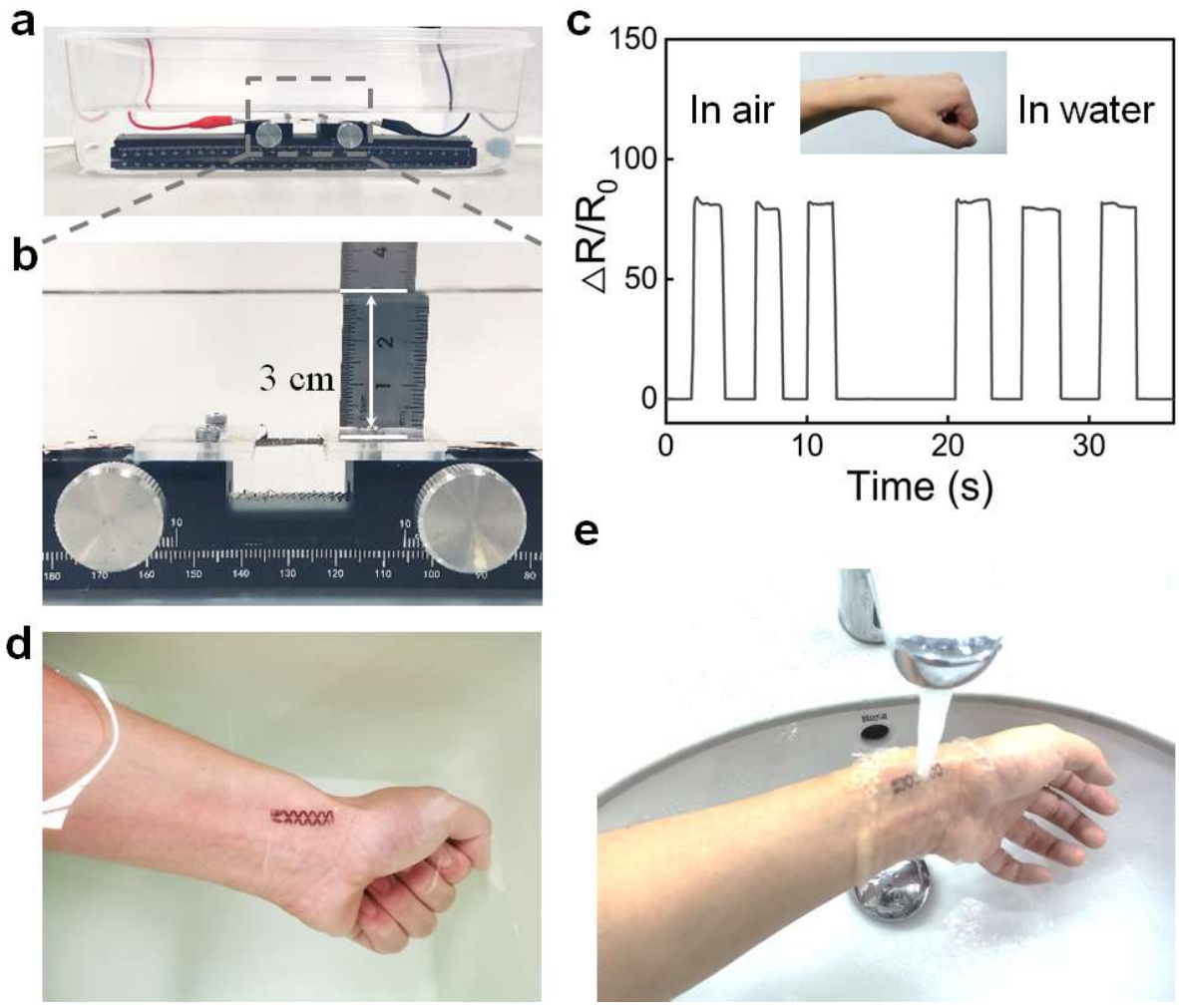

Supplementary Fig. 29. Resilience of strain sensor to water exposure. a), b) The strain sensor was placed on a biaxial mechanical tensile apparatus and immersed in water during tensile testing. **c)** Strain sensors were attached to wrists to measure electrical responses in both water and air. **d)** A photograph of the strain sensor under water. **e)** A photograph of the strain sensor conformally in contact with skin and exposed to water impingement.

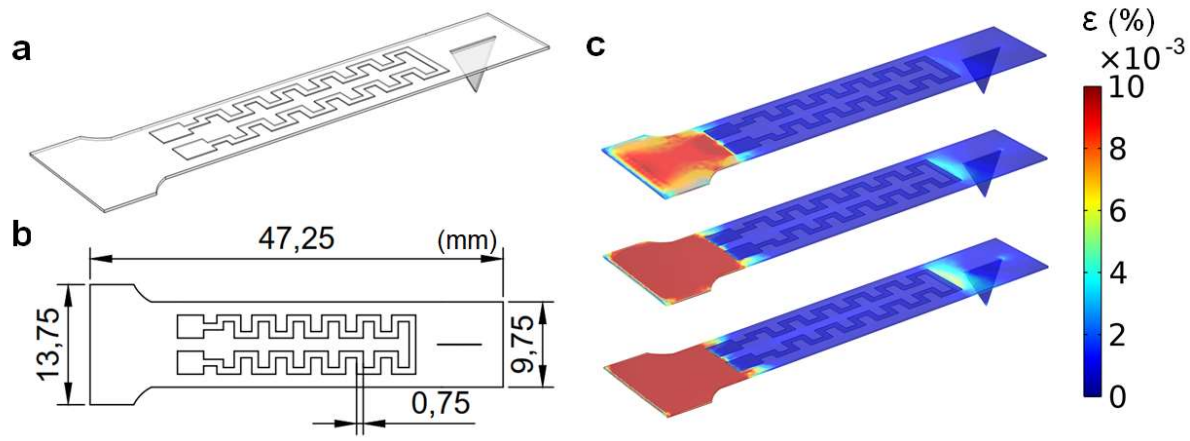

Supplementary Fig. 30. FEA simulated strain distribution in the indirect contact testing mode. The simulation results indicate that, under minor surface variations, the strain changes experienced by the sensor due to cantilever beam conduction are minimal. This highlights the necessity for the sensor to possess exceptionally high sensitivity to effectively detect subtle undulating structures.

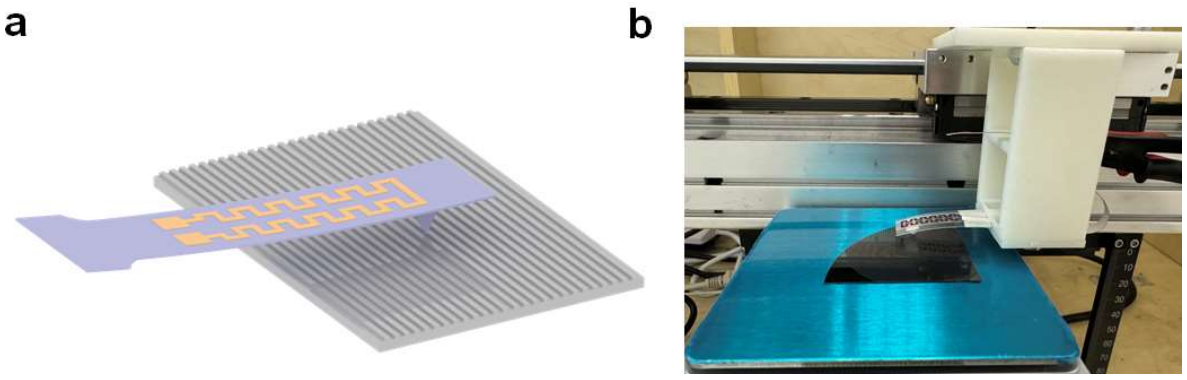

411

412 **Supplementary Fig. 31. Schematic illustration and photograph of the indirect contact**

413 **testing mode.** This figure depicts the setup utilized for indirect contact testing, showcasing

414 both the schematic design and a corresponding photograph of the apparatus.

415

416

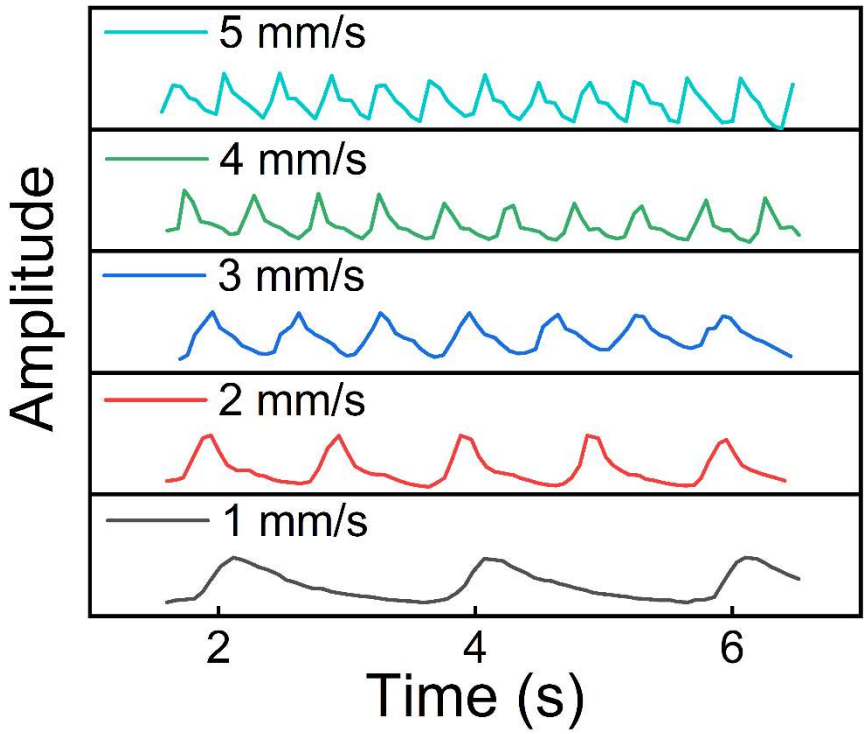

Supplementary Fig. 32. Time domain signals by sliding the sensor on the patterns (height: 300 μm) at five different sliding rates.

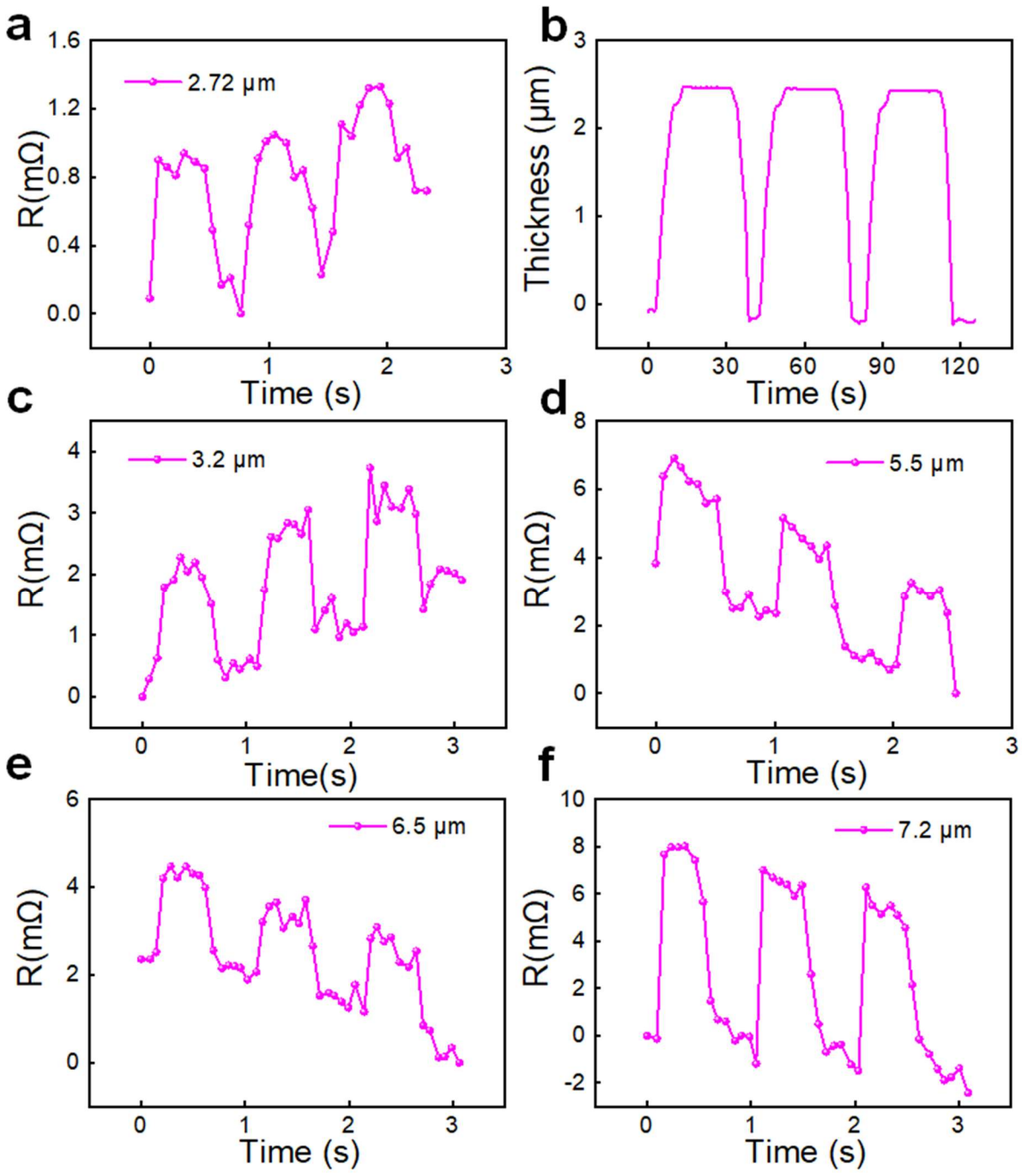

421

422 **Supplementary Fig. 33. Sensing performance of the indirect contact testing mode under**

423 **different heights. a), b)** The height resolution of the strain sensor and height value calibrated

424 by the step gauge. **(c-f)** Sensing performance of the strain sensor in indirect contact mode with

425 patterns of different heights.

426

Supplementary Video 1

Stress distribution across various multiscale heterointerfaces under uniaxial tension. This video visualizes the stress distribution in different heterointerfaces during uniaxial tension.

Supplementary Video 2

Mechanical robustness testing of the flexible electrode with a multiscale heterointerface. This video illustrates the ability of the multiscale heterointerface to withstand harsh mechanical conditions, including scratching, adhesion, and abrasion.

Supplementary Video 3

Observation of crack propagation under *in-situ* uniaxial tensile. This video demonstrates the parallel propagation of cracks on a multiscale heterointerface under uniaxial tension, with crack widths widening as strain increases and gradually narrowing during retraction.

Supplementary Video 4

Stress and strain distributions of multiscale heterointerfaces with varying micropyramid densities. This video illustrates how microstructures serve as stress concentration points and fracture sources, with significant strain localization improvements observed as micropyramid density increases.

Supplementary Video 5

Resilience to pressure disturbances on the multiscale heterointerface of the strain sensor. This video demonstrates the robustness of the heterointerfaces in the strain sensor, which maintains nearly unchanged sensing performance even after being run over by a car.

3. References and notes

1 Wen, L., Xu, R., Mi, Y. & Lei, Y. Multiple nanostructures based on anodized aluminium oxide templates. *Nat. Nanotechnol.* **12**, 244 (2017).

2 Ma, C. *et al.* Robust Flexible Pressure Sensors Made from Conductive Micropyramids for Manipulation Tasks. *ACS Nano* **14**, 12866-12876 (2020).

3 Roy, E. *et al.* Microlens array fabrication by enhanced thermal reflow process: Towards efficient collection of fluorescence light from microarrays. *Microelectron. Eng.* **86**, 2255-2261 (2009).

4 Amjadi, M., Pichitpajongkit, A., Lee, S., Ryu, S. & Park, I. Highly Stretchable and Sensitive Strain Sensor Based on Silver Nanowire–Elastomer Nanocomposite. *ACS Nano* **8**, 5154-5163 (2014).